Available online at www.sciencedirect.com
ScienceDirect
Trans. Nonferrous Met. Soc. China 32(2022) 1530−1547
Transactions of Nonferrous Metals Society of China
www.tnmsc.cn

Low cycle fatigue behavior of zirconium−titanium−steel composite plate

Bin-bin ZHOU[1], Peng YU[1], Le CHANG[2,3], Chang-yu ZHOU[2,3], Cheng YE[4], Bo-jun ZHANG[4]

1. Engineering Technology Training Center, Nanjing Vocational University of Industry Technology, Nanjing 210023, China;
2. School of Mechanical and Power Engineering, Nanjing Tech University, Nanjing 211816, China;
3. Jiangsu Key Lab of Design and Manufacture of Extreme Pressure Equipment, Nanjing 210028, China;
4. Technology Research and Development Department, Nanjing Boiler and Pressure Vessel Inspection Institute, Nanjing 210028, China

Received 15 April 2021; accepted 26 September 2021

Abstract: The low cycle fatigue behavior of zirconium−titanium−steel composite plate under symmetrical and asymmetric stress control was studied. The effects of mean stress and stress amplitude on cyclic deformation, ratcheting effect and damage mechanism were discussed in detail. The results show that under symmetric stress control, the forward ratcheting deformation is observed. Under asymmetric stress control, the ratcheting strain increases rapidly with mean stress and stress amplitude increasing. Under high stress amplitude, the influence of mean stress is more significant. In addition, by studying the variation of strain energy density, it is found that the stress amplitude mainly promotes the fatigue damage, while the mean stress leads to the ratcheting damage. In addition, fractographic observation shows that the crack initiates in the brittle metal compound at the interface, and the steel has higher resistance to crack propagation. Finally, the accuracy of life prediction model considering ratcheting effect is discussed in detail, and a high-precision life prediction model directly based on mean stress and stress amplitude is proposed.

Key words: zirconium−titanium−steel composite plate; low cycle fatigue behavior; fatigue damage; mean stress; ratcheting effect; life prediction model

1 Introduction

In the field of petrochemical and nuclear power equipment, explosive welding metal is often made into vessels, pipelines and transition joints. In recent years, zirconium−titanium−steel explosive welding composite plate is more and more widely used because it can both meet the requirements of structural strength and corrosion resistance at the same time [1,2].

The alternating pressure or dynamic load of transition joints in vessels will cause fatigue damage [3−5]. The existence of interface will greatly affect the resistance to fatigue damage and crack initiation position of composite plates, so fatigue life and crack initiation location have been widely studied [6,7]. The microstructure and properties of AA6061−AA7050 under low cycle fatigue (LCF) were quantitatively studied by RODRIGUEZ et al [8]. Fractographic observation showed that the crack originates from secondary intermetallic compounds near the surface of welding position. In addition, relevant studies showed that the inhomogeneous interface structure in composite plates has a significant effect on the initiation and propagation of fatigue cracks [9−12]. PRAZMOWSKI et al [13] found that crack always initiates at the steel side and then extends to the titanium side. SNIEZEK et al [14] found that the

Corresponding author: Chang-yu ZHOU, Tel: +86-25-58139951, E-mail: changyu_zhou@163.com
DOI: 10.1016/S1003-6326(22)65891-6

fatigue life of composite plate would be greatly improved by choosing appropriate heat treatment process, and the crack initiation position would change from interface to substrate. At present, the LCF tests of titanium−steel, zirconium−steel composite plates are mainly focused on crack initiation location and fatigue life under symmetrical stress control. There is a lack of research on fatigue behavior for composite plate under asymmetric stress control.

Engineering components and structures often bear cyclic stress with mean stress (σ_m), which has great influence on fatigue life [15−17]. At present, the effect of σ_m has been widely studied. For fatigue life, studies [18,19] show that mean tensile stress is unfavorable to fatigue life, and mean compressive stress is beneficial to fatigue life. However, studies show that the influence of σ_m on material deformation characteristics needs to be explored before analyzing the contribution of σ_m to fatigue life [20,21]. For micro-deformation mechanism of materials, the influence of ratcheting effect can be evaluated by studying the evolution of dislocation structure in materials under asymmetric loads [22,23]. For life prediction model, in order to evaluate the effect of σ_m, various life prediction models considering σ_m have been proposed, such as Gerber model, Goodman model, Soderberg model, Morrow model and Walker model. INCE [24] proposed a fatigue damage model based on distorted strain energy, and compared it with Morrow and SWT correction models. MAHTABI and SHAMSAEI [25] studied the fatigue behavior of NiTi alloy and proposed an energy-based fatigue model, where the effects of mean tensile strain and stress on fatigue resistance were considered.

At present, the research on LCF behavior of zirconium−titanium−steel composite plate under asymmetric fatigue loading has less been reported, which limits further application of zirconium−titanium−steel composite plate. Therefore, the cyclic deformation characteristics, ratcheting effect and damage mechanism of zirconium−titanium−steel composite plate need to be studied in detail. Moreover, the current life prediction model considering σ_m has the disadvantage that the parameters are complex and depend too much on the loading cycle characteristics. Thus, it is of great significance to study life prediction model with large accuracy under asymmetric stress control, which is directly based on the loading parameters.

2 Experimental

The test material is zirconium−titanium−steel explosive composite plate. The material grade and chemical composition are given in Tables 1−3. Fatigue specimens were fabricated from large size composite plate by wire cutting along the direction perpendicular to the rolling direction. The material was taken away from the central explosion point and the edge position. The specimen size of zirconium−titanium−steel composite plate is shown in Fig. 1. There are three kinds of materials in the thickness direction of composite plate, among which Zr702 is used as cladding material with thickness of about 2 mm, Q345R steel is used as base material with thickness of 8.2 mm, and TA2 is used as transition material with thickness of about 1.8 mm. Due to the influence of material deformation and explosive welding process, there are some errors in the thickness of each layer, and the total thickness of the LCF specimen is kept at 12 mm. Before fatigue test, the samples were polished, and the cross-sectional dimensions of the final samples were recorded.

LCF test has triangular loading waveform, which was stress-controlled and carried out on

Table 1 Chemical composition of Zr702 (wt.%)

Zr+Hf	Hf	Fe+Cr	H	N	C	O	Nb
≥99.2	4.5	0.2	0.005	0.025	0.05	0.16	−

Table 2 Chemical composition of TA2 (wt.%)

Fe	C	N	H	O	Other	Ti
0.3	0.1	0.05	0.015	0.25	0.5	Bal.

Table 3 Chemical composition of Q345R (wt.%)

C	Si	Mn	P	S	Fe
0.15	0.39	1.43	0.018	0.005	Bal.

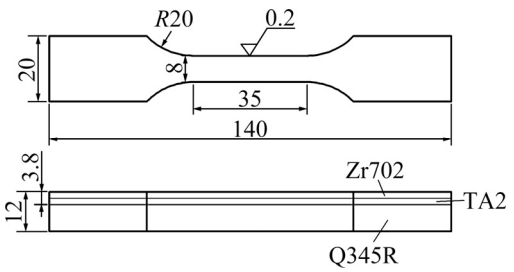

Fig. 1 Dimension of LCF specimens of zirconium−titanium−steel composite plate (Unit: mm)

MTS809 hydraulic testing machine. The stress rate is kept constant at 600 MPa/s in all tests. Fatigue tests are divided into symmetrical stress-controlled and asymmetrical stress-controlled ones. For symmetrical stress-controlled test, stress amplitude (σ_a) values are 290, 310, 340 and 370 MPa, while σ_a values are 310, 340 and 370 MPa for asymmetrical stress-controlled test. Each group of σ_a considers three groups of σ_m. The specific test scheme is given in Table 4, where N_f represents fatigue life. The strain magnitude corresponding to the half-life period is given in Table 4.

Table 4 Low-cycle fatigue test parameters of zirconium−titanium−steel composite plate

Control	Sample	ε_a/%	σ_a/MPa	σ_m/MPa	N_f
Symmetrical stress	P01	0.190	290	0	50695
	P02	0.274	310	0	12553
	P03	0.321	340	0	7750
	P04	0.461	370	0	2490
Asymmetrical stress	P05	0.266	310	10	12940
	P06	0.323	310	30	4600
	P07	0.279	310	50	2499
	P08	0.349	340	10	5375
	P09	0.453	340	30	2536
	P10	0.428	340	50	1222
	P11	0.498	370	10	3730
	P12	0.482	370	30	1858
	P13	0.561	370	50	686

3 Results and discussion

3.1 Symmetrical stress control

3.1.1 Cyclic softening behavior

The relationship between nominalized fatigue cycle number (N/N_f) and strain range is shown in Fig. 2(a). The strain range is twice the strain amplitude, that is, $2\varepsilon_a$. Figure 2(a) shows that $2\varepsilon_a$ increases with N, that is, the composite plate shows cyclic softening. With the increase of N, $2\varepsilon_a$ tends to be stable until crack or fracture occurs in the final stage. In addition, with the increase of $2\varepsilon_a$, the cyclic softening phenomenon in the initial stage of loading becomes more and more obvious, and the loading cycles entering the stable stage are postponed in the whole life cycle. In fact, cyclic softening is related to the evolution of dislocation structure during cyclic loading. For cyclic softening materials, dislocation structures generated under cyclic loading annihilate with the increase of N, which is usually considered dislocation recovery process. Therefore, this leads to the decrease of dislocation density and slip resistance in cyclic deformation. In addition, dislocation substructures with complex structures may be rearranged, or reconstructed, to form new dislocation configurations with less fatigue resistance [22]. Therefore, under constant stress control, $2\varepsilon_a$ of materials increases with the change of dislocation structure, i.e. cyclic softening. It can be seen that with the increase of σ_a, the annihilation and reconstruction process of dislocation structure is more significant, so the cyclic softening characteristics of the whole material are more obvious.

In stress-controlled fatigue tests, dimensionless softening coefficient, H_σ, is used to describe cyclic softening behavior:

$$H_\sigma = \frac{\varepsilon_a - \varepsilon_s}{\varepsilon_a} \tag{1}$$

where ε_s represents the strain corresponding to the half-life cycle.

Figure 2(b) shows that the cyclic softening behavior under different σ_a can be divided into three stages. $0.5N_f$ and the previous loading cycles belong to the first stage. During this stage, H_σ of composite plate increases rapidly, and the increasing speed decreases with N. In addition, the increase of σ_a significantly increases the increase rate of H_σ. After $0.5N_f$, H_σ increases slowly in the second stage, and H_σ in this stage is not affected by σ_a. Finally, the third stage is the initiation and propagating stage of the crack, which causes rapid failure, and H_σ increases sharply. Figure 2(b) shows that the loading cycles are very few in this stage, and the proportion of loading cycles to the whole life cycle increases slightly with σ_a.

Figure 2(c) shows the change of plastic strain range ($2\varepsilon_a^p$). It can be seen that $2\varepsilon_a^p$ increases significantly with σ_a. The variation law is consistent with that of $2\varepsilon_a$. In fact, the cyclic damage of materials is mainly related to the accumulation of cyclic plastic strain [26]. The higher the σ_a is, the higher the plastic deformation occurs under each loading cycle, and the higher the damage accumulation is, so the damage occurs earlier.

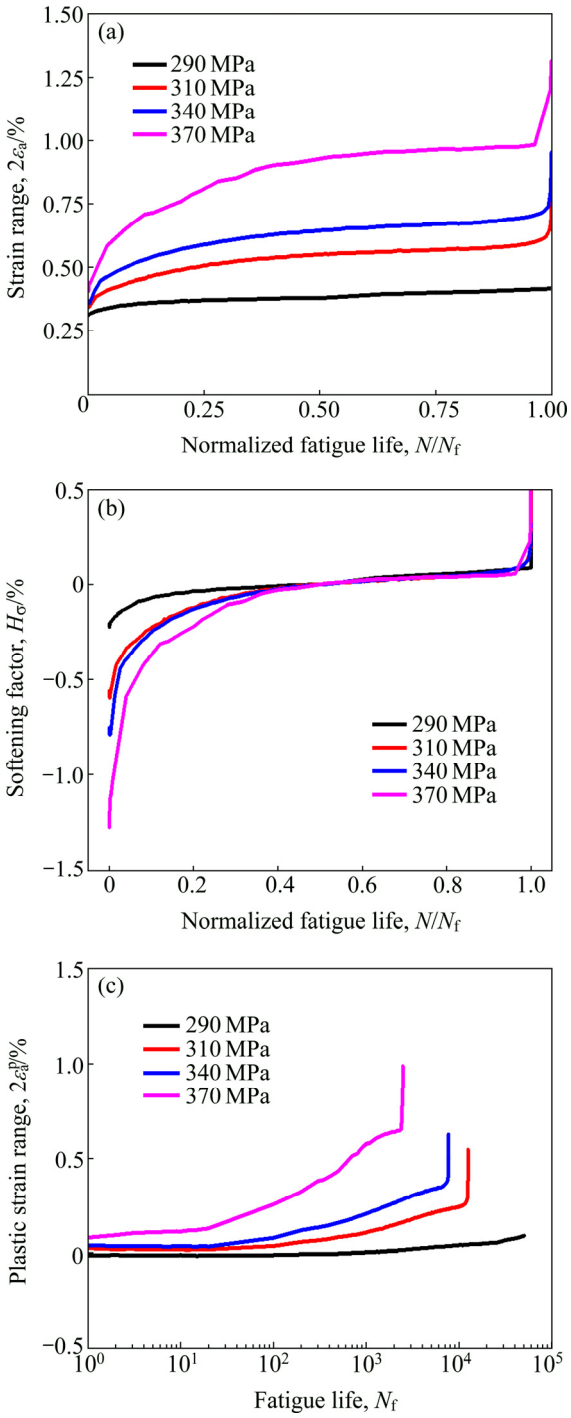

Fig. 2 Variations of $2\varepsilon_a$ (a), H_σ (b) and $2\varepsilon_a^p$ (c) in LCF test under symmetrical stress control

3.1.2 Ratcheting deformation

Because of the asymmetric compression, even under symmetrical stress control, ε_m of most materials gradually shifts, which is called ratcheting deformation [26]. In fatigue tests, ratcheting strain ε_r is defined as one-half of the sum of maximum strain and minimum strain, i.e. $\varepsilon_r=(\varepsilon_{max}+\varepsilon_{min})/2$. It is generally believed that ε_r is unfavorable to fatigue life. ε_r promotes the accumulation of non-uniform plastic strain in material cyclic deformation, aggravates the damage and accelerates the crack initiation. After the crack initiation, ratcheting deformation causes crack tips to keep open at all time, and crack closure decreases, resulting in an increase in the actual stress intensity factor, which promotes crack propagation [18]. Figure 3 shows that ε_r is offset in LCF test under symmetrical stress control, and the offset degree is remarkable with the increase of σ_a. It can be seen that the compressive deformation resistance of zirconium−titanium−steel composite plate is greater than the tensile deformation resistance, so with the increase of N, ε_m increases, and the ratcheting deformation is more significant.

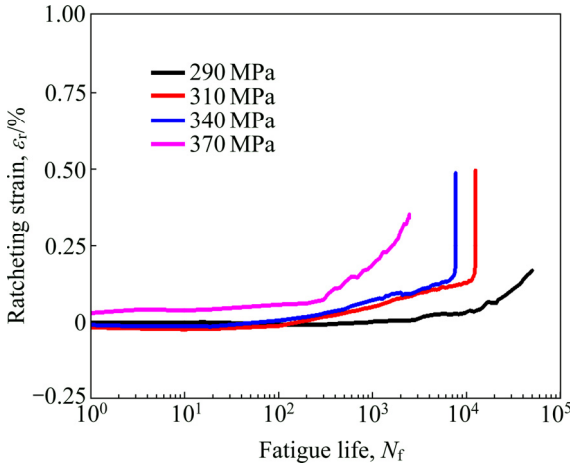

Fig. 3 ε_r in LCF tests under symmetrical stress control

3.2 Asymmetric stress control

Current studies [14,15] show that the main factors for ratcheting effect are the cyclic hardening/softening deformation characteristics, loading conditions and viscoplasticity of materials. In engineering practice, the loads on materials and components are usually asymmetric, that is, there is an effect of σ_m, so ε_r is generated along the direction of σ_m. The ε_r caused by σ_m has an important influence on fatigue life, so it needs to be considered in safety design and life evaluation. For zirconium−titanium−steel composite plate, cladding layer (zirconium) and transition layer (titanium) are more sensitive to σ_m than base steel, so ratcheting effect is more significant [11].

3.2.1 Effect of mean stress (σ_m)

Figure 4 shows the effect of σ_m on $2\varepsilon_a$ and ε_r. When σ_a is low (Fig. 4(a)), $2\varepsilon_a$ increases gradually with σ_m, but the promotion effect is limited. When

σ_a is high (Fig. 4(b)), the increase of σ_m greatly contributes to $2\varepsilon_a$, and the strain promotes the accumulation of plastic strain and cyclic damage, so the fatigue life decreases greatly. The variation trend of ε_r in Figs. 4(c, d) shows that ε_r increases greatly with σ_m under different σ_a, and the difference between ε_r under different σ_m increases with loading cycles. In addition, the effect of σ_m on $2\varepsilon_a$ and ratcheting effect is more significant at high ε_a.

In Fig. 5, under low σ_a, $2\varepsilon_a$ of hysteretic curves under different σ_m is similar under the same loading cycle, but ε_m increases significantly. With the increase of loading cycles, the change of ε_m is more significant than that of $2\varepsilon_a$. In the case of high σ_a, $2\varepsilon_a$ and ε_m of hysteretic curves under different σ_m increase greatly in the same loading cycle, and the increase of ε_m is more obvious. Moreover, the

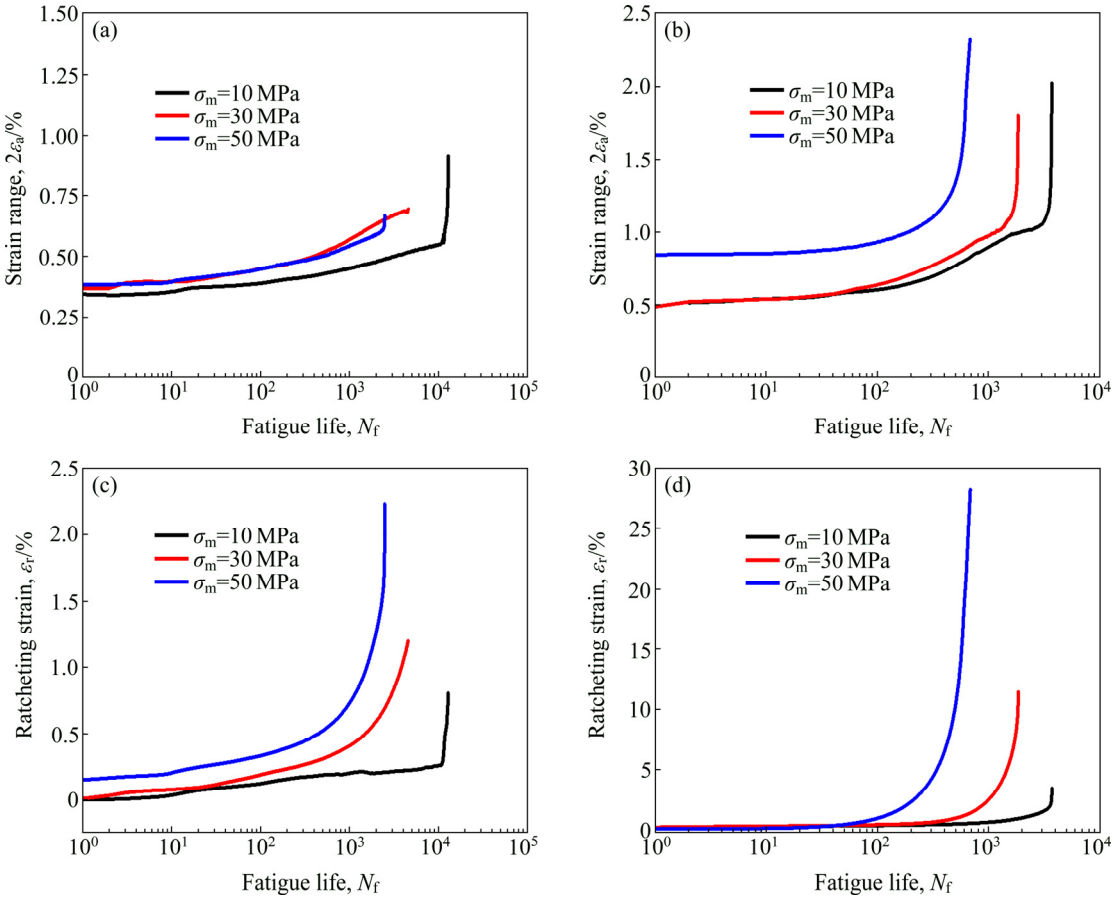

Fig. 4 Influence of σ_m on $2\varepsilon_a$ (a, b) and ε_r (c, d): (a, c) σ_a=310 MPa; (b, d) σ_a=370 MPa

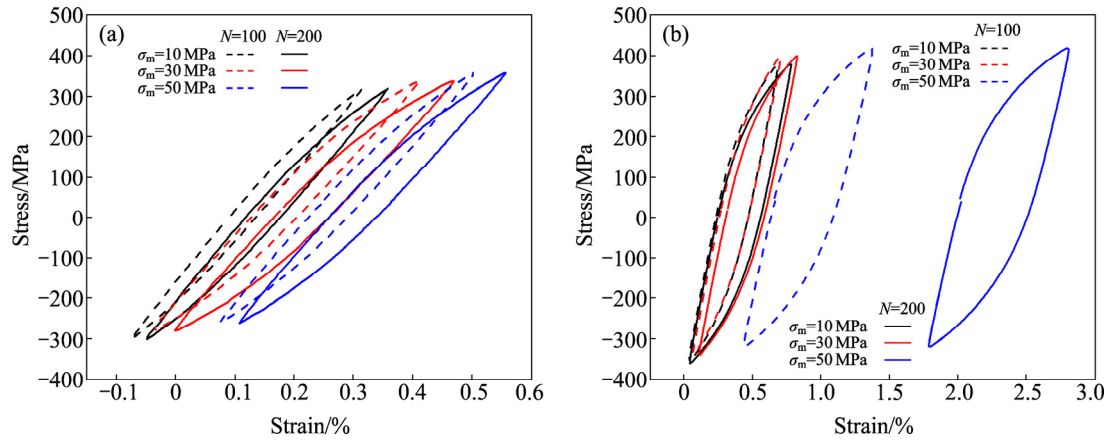

Fig. 5 Influence of σ_m on hysteresis curve: (a) σ_a=310 MPa; (b) σ_a=370 MPa

change of $2\varepsilon_a$ under different σ_m is not obvious, while ε_m is greatly increased. It can be seen that under high σ_a, the increase of σ_m has more significant effect on ratcheting effect, and the difference of ε_r is enlarged with the increase of loading cycles.

Compared with the low σ_a, the cyclic softening behavior of the material is more obvious under the high σ_a and $2\varepsilon_a$ changes more greatly, so the cumulative plastic deformation under single cyclic loading is higher. When the material is subjected to additional σ_m, the non-uniform plastic deformation of the material becomes more significant, which results in the rapid accumulation of ε_r.

3.2.2 Effect of stress amplitude (σ_a)

Figure 6 shows the effect of σ_a on $2\varepsilon_a$ and ε_r under different σ_m. Figures 6(a, b) show that the increase of σ_a leads to the increase of $2\varepsilon_a$. Figures 6(c, d) show that when σ_m and σ_a are low, ε_r increases slightly with σ_a. The higher the σ_m is, the more obvious the effect of σ_a on ε_r is. It can be seen that the effect of σ_a on ratcheting effect is affected by σ_m. Only when σ_m reaches a certain level, the effect of σ_a on ratcheting stress is significant enough. This is because ε_r is mainly caused by σ_m during cyclic loading. Although the increase of σ_a promotes the increase of $2\varepsilon_a$, ε_r is very small when σ_m is low, so the cumulative difference of ε_r is not obvious.

In Fig. 7, when σ_m is low, σ_a promotes the increase of $2\varepsilon_a$, but when the loading cycles are small, the effect on ε_m is not clear, and with the increase of the loading cycles, the overall offset of the hysteretic curve is also limited. When σ_m is higher, $2\varepsilon_a$ and ε_r increase significantly with σ_a, and ε_r increases more obviously with loading cycles. It can be seen that ε_r is more sensitive to the change of σ_a when σ_m is higher.

3.2.3 Energy analysis

Strain energy density is an important parameter for describing damage evolution during cyclic deformation. In the process of cyclic deformation, the elasticity, plasticity and total strain energy density can be obtained by analyzing the hysteresis curve, i.e. the stress−strain curve. Among them, plastic strain energy density is considered to

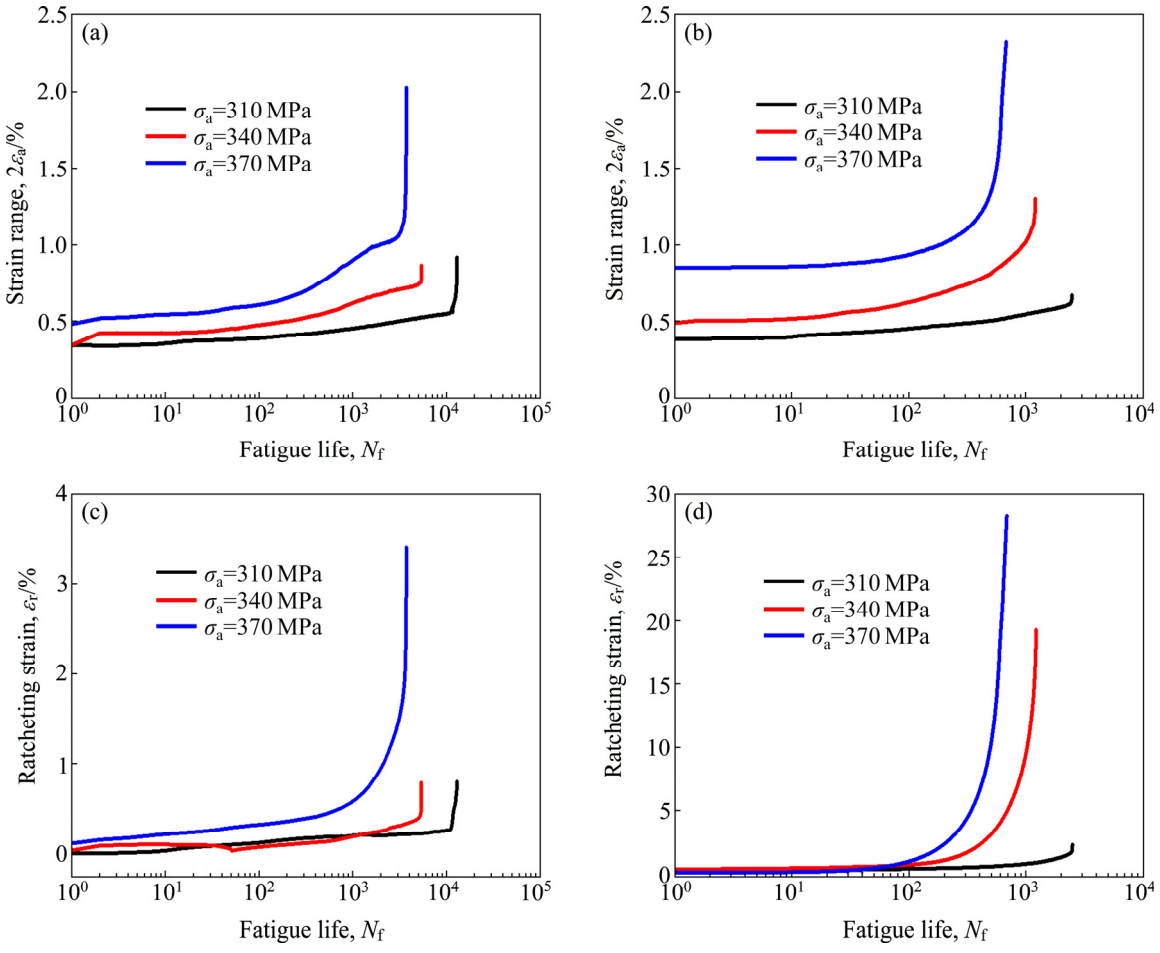

Fig. 6 Effect of σ_a on $2\varepsilon_a$ (a, b) and ε_r (c, d): (a, c) σ_m=10 MPa; (b, d) σ_m=50 MPa

be the most important parameter to cause material damage, so it is widely used in fatigue life prediction. The formula for calculating strain energy density considering stress ratio is as follows:

$$\Delta W_t=\Delta W_p+\Delta W_e^+ \tag{2}$$

$$\Delta W_p=\int_{\varepsilon_{p1}}^{\varepsilon_{p2}}\sigma \mathrm{d}\varepsilon_p \tag{3}$$

$$\Delta W_e^+=\frac{\sigma_p^2(1-R)^2}{2E}+\Delta\sigma_{min}\Delta\varepsilon \quad (R\geq 0) \tag{4}$$

$$\Delta W_e^+=\frac{\sigma_p^2}{2E} \quad (R<0) \tag{5}$$

where ΔW_t denotes the total strain energy density; ΔW_p and ΔW_e^+ denote the plastic strain energy density and the elastic strain energy density, respectively; R represents the stress ratio and E represents the elastic modulus.

Figure 8 shows that the ΔW_p change of zirconium−titanium−steel composite plate during cyclic deformation can be divided into three stages: the first stage is rapid rising stage, the second stage is relatively stable stage, and the third stage is rapid failure stage. In Fig. 8(a), with the increase of σ_m, the ΔW_p increases, and when σ_m is 30 MPa, the increase of ΔW_p under initial cyclic loading cycles is limited compared with that under the condition with σ_m of 10 MPa. From the results of the influence of σ_m on $2\varepsilon_a$ and ε_r, it can be seen that the ratcheting effect of materials is not obvious under initial cyclic loading cycles when σ_m increase is not obvious, and the cumulative degree of plastic strain mainly depends on the magnitude of stress range, so the increase of ΔW_p is limited. In the third stage, cracks initiate, and the change of ΔW_p here is significantly affected by the crack growth rate and propagation path, so the variation is different from that of the first two stages. In Fig. 8(b), the effect ofσ_a increase on ΔW_p is consistent with σ_m, and the difference of ΔW_p results under different σ_a is more significant. Therefore, the increase of σ_a directly increases $2\varepsilon_a$, leading to a significant increase of ΔW_p. When σ_a is fixed, the influence of σ_m on ΔW_p depends on the contribution of ratcheting effect caused by σ_m to the accumulation of cyclic plastic strain.

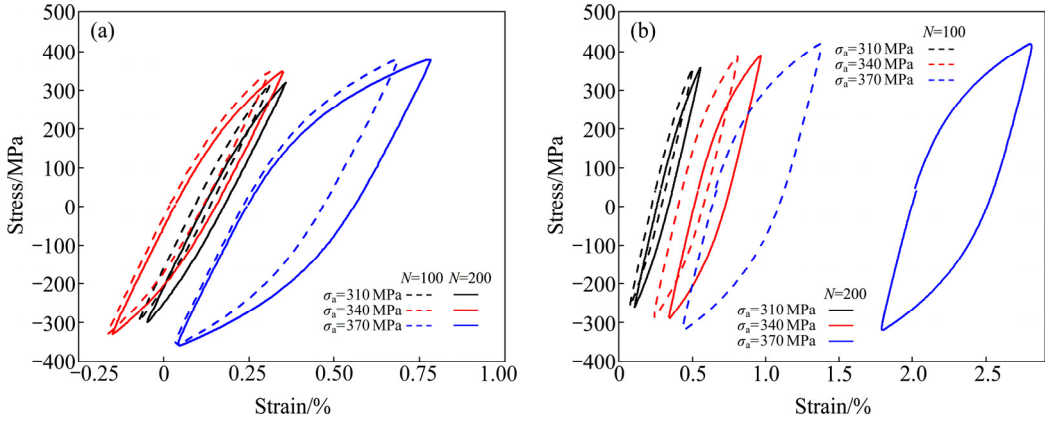

Fig. 7 Effect of σ_a on hysteresis curve: (a) σ_m=10 MPa; (b) σ_m=50 MPa

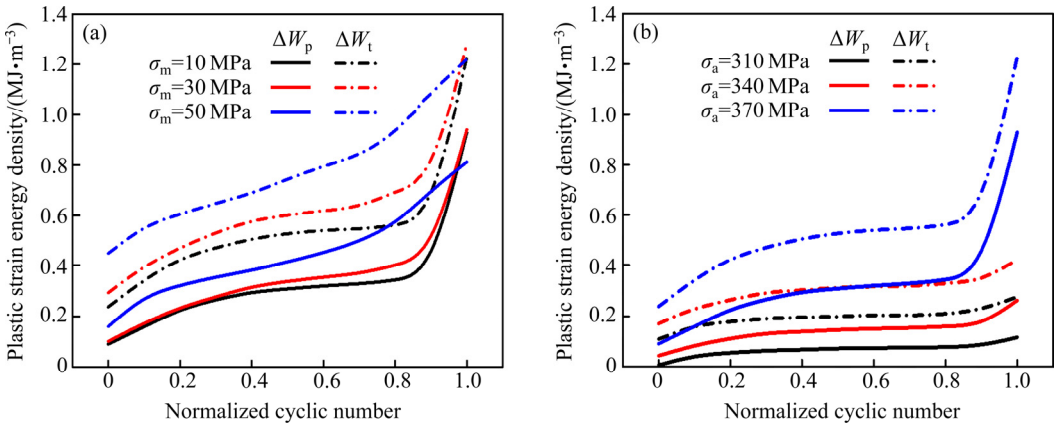

Fig. 8 Variations of ΔW_p and ΔW_t with σ_m (a) and σ_a (b): (a) σ_a=370 MPa; (b) σ_m=10 MPa

Figure 9 shows the effect of σ_m and σ_a on proportions of ΔW_p and ΔW_e^+ in ΔW_t. Although σ_m increases ε_r and cyclic plastic strain accumulation, its effect on the proportions of ΔW_p and ΔW_e^+ in ΔW_t is limited, even negligible. The effect of σ_m on material hysteresis curves shows that with the increase of σ_m, the hysteresis curve of material moves towards the direction of σ_m, but $2\varepsilon_a$ and the area ΔW_p enclosed by the hysteresis curve are almost unchanged. This is the reason why the proportion of ΔW_p and ΔW_e^+ in ΔW_t does not change obviously as σ_m increases. In Fig. 9(b), with the increase of σ_a, the proportion of ΔW_p in ΔW_t increases rapidly, while the proportion of ΔW_e^+ in ΔW_t decreases correspondingly, which indicates that the increase of σ_a directly causes the increase of ΔW_p, and increases the plastic strain accumulation under each cycle loading. Similarly, the effect of σ_a on hysteretic curve verifies this view, that is, the increase of σ_a increases $2\varepsilon_a$ and the area of ΔW_p enclosed by hysteretic curve. It can be seen that the contribution of σ_m to material damage is mainly ratcheting damage, while the increase of σ_a mainly increases the proportion of ΔW_p, and the cyclic plasticity cumulative degree under each cyclic loading, thus causing fatigue damage.

3.3 Fractographic observation of fracture surface

Figure 10(a) shows that the fracture surfaces of titanium and zirconium are smooth and identified as stable and rapid crack growth zones, respectively. In steel, flat crack growth zones account for a small proportion of the overall area, and most of the steel is in instantaneous fracture zone. This indicates that the crack propagates to both sides of the material after the initiation of structure in vortex zone, and its growth rate in titanium and zirconium is significantly higher than that in steel. It can be seen that the crack propagation resistance of steel is higher than that of titanium and zirconium, so the instantaneous fracture zone only exists in steel. During explosive welding, adiabatic shear occurs at the explosive point, and the resulting jet particles are quickly extruded and cooled by the sheet metal, which results in formation of fine grains in melting state at high temperature without recrystallization and grain growth [27]. Figures 10(b, c) show that intergranular fracture occurs in the fine grain zone of steel, which indicates that the grain strength of the fine grain zone is higher than the grain boundary bonding strength, leading to crack propagation along the grain boundary under fatigue load. The crack source region of titanium has cleavage-like morphology, which indicates that transgranular brittle fracture occurs.

The morphologies of the stable crack growth zone in each layer are shown in Figs. 10(d, e, f). In zirconium, obvious fatigue striations can be observed in the superficial dimples. The appearance of dimples indicates that the ductile fracture characteristics begin to accompany the crack propagation process, and the tearing edges everywhere also indicate that the plastic deformation of the crack tip is obvious. Compared with the cracks in titanium, the actual driving force of crack tip propagation is higher and propagation speed is faster. Fatigue striations and tearing edges are ubiquitous in titanium. Fatigue striation is typical of fatigue damage. Tearing edges indicate that crack propagation in titanium contains a small amount of plastic deformation. In steel, the secondary cracks and the plastic deformation

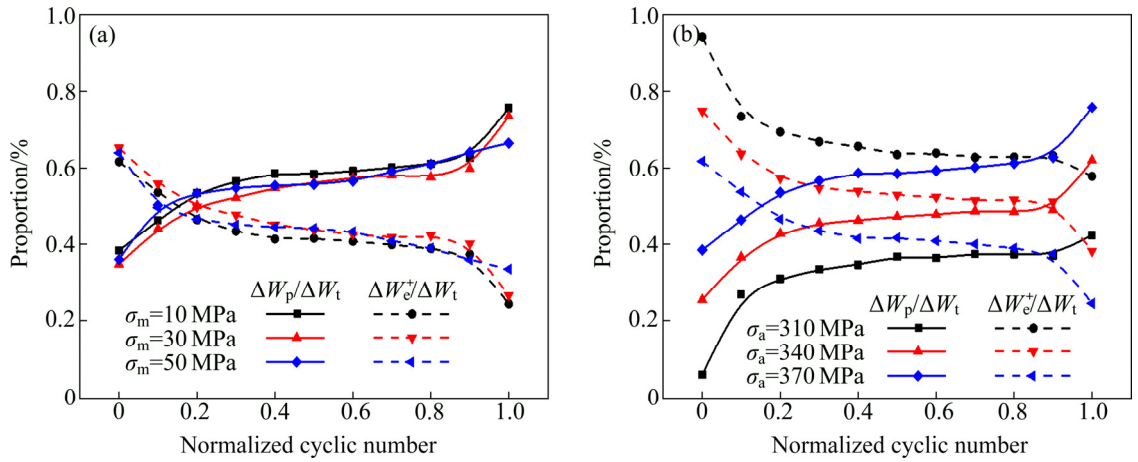

Fig. 9 Effect of σ_m (a) and σ_a (b) on proportions of ΔW_p and ΔW_e^+ in ΔW_t: (a) σ_a=370 MPa; (b) σ_m=10 MPa

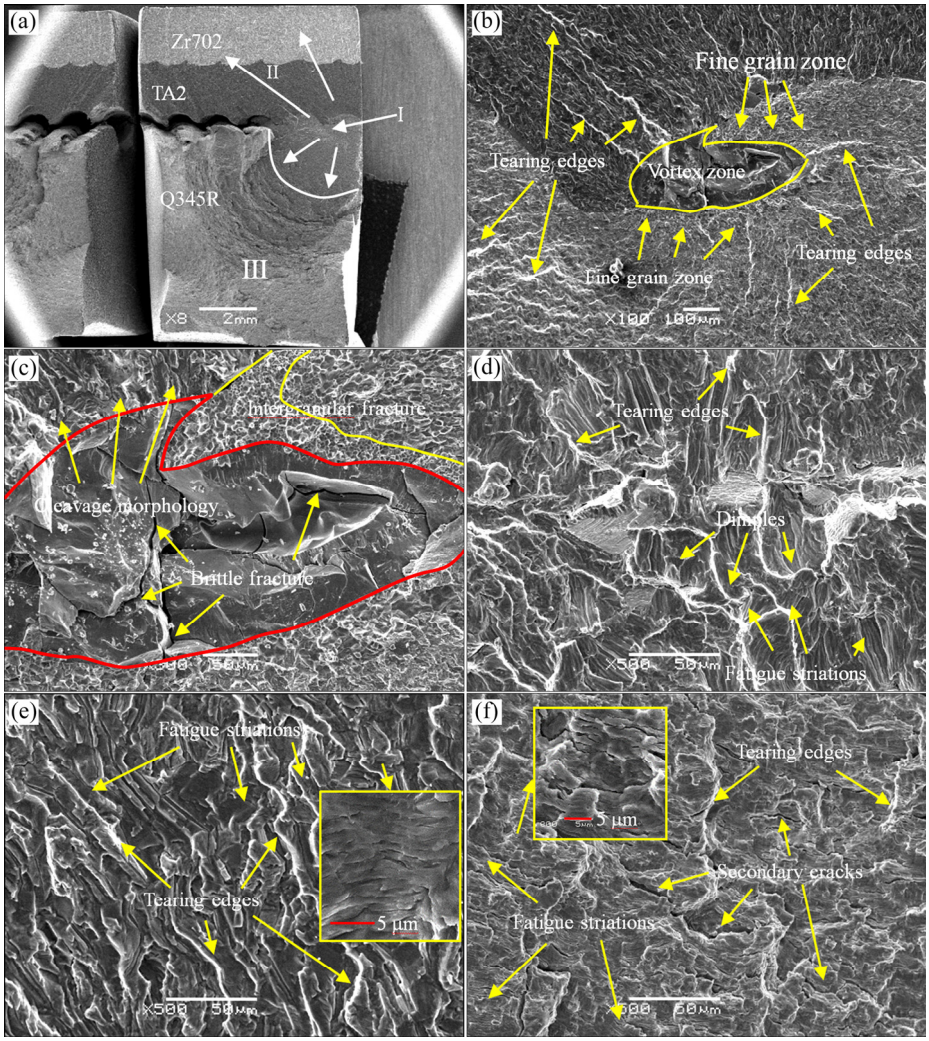

Fig. 10 Fatigue fracture morphologies of zirconium−titanium−steel composite plate under σ_a of 370 MPa: (a) Overall morphology; (b) Titanium−steel bonding interface; (c) Crack initiation point in vortex zone; (d) Stable growth zone of zirconium layer; (e) Stable expansion zone of titanium layer; (f) Stable expansion zone of steel layer

characteristics are obvious, and the fatigue striations are clearer than those in the other two. These characteristics show that when cracks propagate in steel, severe plastic deformation at crack tips tends to produce secondary crack surfaces, but because of its higher resistance to crack propagation and the dispersal of the driving force of crack tip propagation, the crack propagation rate is significantly lower than that in titanium and zirconium, so its stable growth zone is very small. When titanium and zirconium are ompletely separated due to crack propagation, fatigue load leads to rapid crack propagation and instantaneous fracture in steel.

Figure 11 shows fatigue fracture morphologies when σ_a is 370 MPa and σ_m is 50 MPa. In Fig. 11(a), significant plastic deformation occurs at the fracture surface of the whole specimen, which is caused by ratcheting plastic deformation of σ_m. Due to severe plastic deformation, the bonding interface between titanium and steel with significant difference in properties is completely separated, while the interface between titanium and zirconium with similar properties is well bonded. In Fig. 11(b), it is found that the crack initiation is still located in the vortex zone of the titanium−steel bonding interface even when σ_m causes severe plastic deformation. Similarly, in this region, brittle fracture occurs in the compounds of the vortex zone, and the crack initiation position in titanium shows cleavage-like characteristics. The subsequent fracture morphologies of various components show that there is a transient stable crack growth zone in titanium, and the fracture features are fatigue

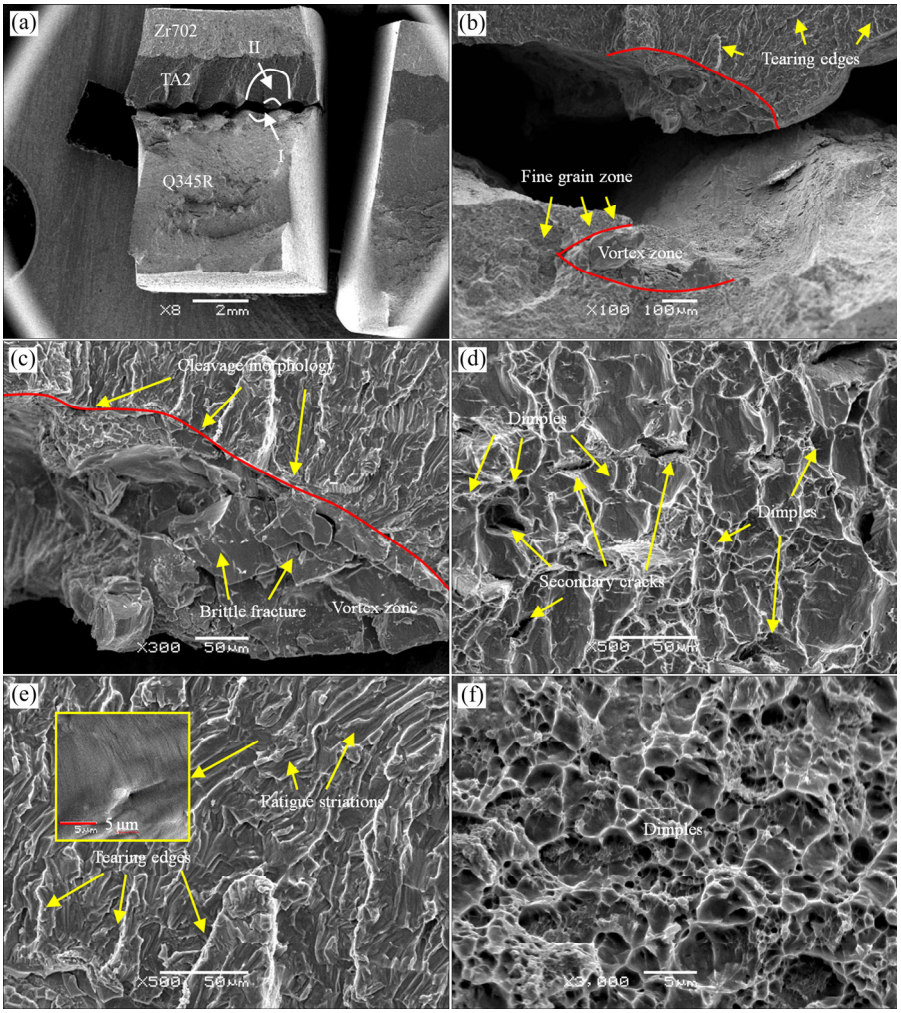

Fig. 11 Fatigue fracture morphologies of zirconium−titanium−steel composite plate under σ_a of 370 MPa and σ_m of 50 MPa: (a) Overall morphology; (b) Titanium−steel bonding interface; (c) Crack initiation point in vortex zone; (d) Stable growth zone of zirconium layer; (e) Stable expansion zone of titanium layer; (f) Stable expansion zone of steel layer

striation and a few tearing edges, as shown in Fig. 11(e). In Figs. 11(d, f), zirconium and steel are filled with dimples, which is a typical ductile fracture mode, and there is no stable crack growth zone.

Therefore, even if the zirconium−titanium−steel composite plate is subjected to relatively large σ_m and thus has obvious plastic deformation, the vortex zone of the titanium−steel interface is still the location of crack initiation. When fatigue load and ratcheting effect are applied, brittle fracture occurs first in this region, and then cracks propagate continuously under ratcheting deformation damage and fatigue damage.

3.4 Life prediction

At present, life prediction models considering σ_a, ratcheting effect and energy-related factors have received extensive attention [25]. In this section, the accuracy of fatigue life prediction for zirconium−titanium−steel composite plate under symmetrical and asymmetrical stress control has been studied by using different models. Based on this, a fatigue life prediction model is proposed, which is related to σ_m and σ_a.

3.4.1 Life prediction model of symmetrical stress control

(1) Basquin model

Basquin model [12], as one of the most basic life prediction methods, is widely used in life prediction of symmetrical loading fatigue test. For symmetrical stress-controlled loading, the model is defined as follows:

$$\sigma_a = \sigma_f' N_f^b \quad (6)$$

where σ_f' represents the fatigue strength coefficient and b represents the fatigue strength index. According to the fatigue life data of symmetrical stress loading in this work, the values of σ_f' and b can be determined, as shown in Fig. 12. Because the Basquin model is simple in structure and completely based on the fitting of test life data, the accuracy of the model is not high when the test data are limited.

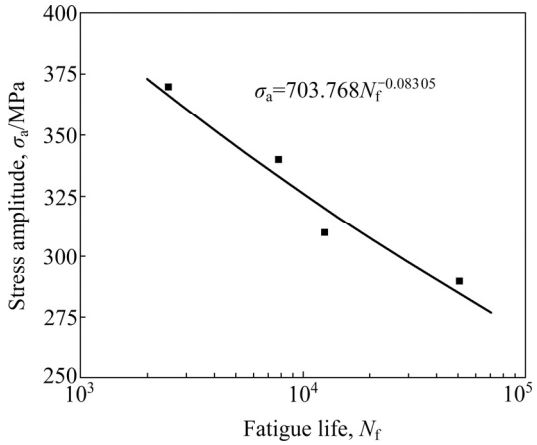

Fig. 12 σ_a and fatigue life curve under symmetrical stress control

(2) Energy-based life prediction model

Because strain energy density can describe the energy dissipation during cyclic deformation, it is applied to life prediction. Generally, for symmetrical loading test, the total strain energy density (ΔW_t) under various loading parameters is obtained by taking the hysteretic curve of material half-life cycle, and the relationship between the total strain energy density ΔW_t and fatigue life is established by the following formula:

$$\Delta W_t = k_f N_f^{\alpha} \tag{7}$$

where k_f and α are material constants, which are obtained by fitting the experimental data. According to the experimental data of P01−P04, the energy-based life prediction model of zirconium−titanium−steel composite plate is shown in Fig. 13. It can be seen that the prediction accuracy of this model is significantly higher than that of the Basquin model.

3.4.2 Life prediction model of asymmetric stress control

In the case of asymmetric loading, the symmetric loading model is no longer applicable because of the existence of σ_m. Therefore, in order to improve the accuracy of fatigue life prediction under asymmetric loading, more life prediction models considering the effects of σ_m, ratcheting effect and strain energy density are proposed.

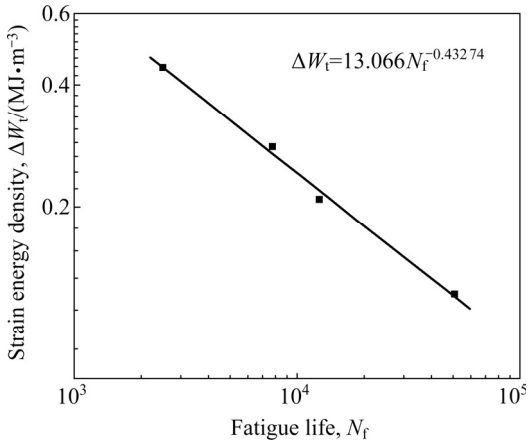

Fig. 13 Total strain energy density ΔW_t and fatigue life curve under symmetrical stress control

(1) Xia model

Under asymmetric loading, σ_m or strain leads to ratcheting deformation. In order to quantitatively describe the contribution of ratcheting deformation to the fatigue life under asymmetric loading, Xia proposed a life prediction model based on linear damage theory, called Xia model. It is considered that the composite Miller damage model of pure fatigue life and ratcheting life is

$$\frac{1}{N_f} = \frac{1}{N_{ff}} + \frac{1}{N_{fr}} \tag{8}$$

where N_{ff} represents pure fatigue life, and N_{fr} represents pure ratcheting life. The pure fatigue life is obtained by referring to the Basquin model under symmetrical loading.

The pure ratcheting life and ratcheting parameters match with the following functional relationship:

$$\sigma_{max}\dot{\varepsilon}_r = k_r N_{fr}^{\beta} \tag{9}$$

where σ_{max} is the peak stress, $\dot{\varepsilon}_r$ is the average ratcheting strain, k_r and β are the material constants. The fatigue life data of asymmetric test are obtained, and the final form of Xia model is obtained:

$$N_f = \left[\left(\frac{13.07}{\Delta W_t}\right)^{-2.31} + \left(\frac{135922}{\sigma_{max}\dot{\varepsilon}_r}\right)^{-0.74}\right]^{-1} \tag{10}$$

Figure 14 shows that the life predicted by Xia model is within the range of twice the error band, and the accuracy meets the requirements.

(2) Life prediction model based on equivalent stress amplitude

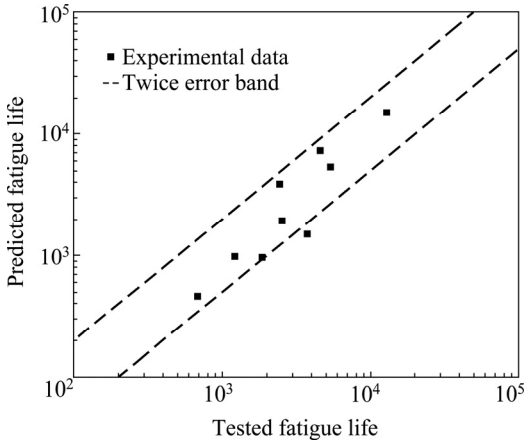

Fig. 14 Comparison of predicted and tested fatigue life data of Xia model

In order to consider the effect of σ_m on fatigue life, a life prediction model considering equivalent stress amplitude σ_{eq} is proposed. In this model, the σ_{eq} equation considering σ_a, σ_m and σ_{max} is established to replace σ_a in the general power law life model, and the life model considering the influence of σ_m is obtained. Goodman model [28], SWT model [29], Walker model [30] and Kwofie model [31] are widely used in this kind of model.

In Goodman model, σ_{eq}, σ_a, σ_m and tensile strength σ_u have the following relationship:

$$\sigma_{eq.G}=\frac{\sigma_a}{1-\sigma_m/\sigma_u} \tag{11}$$

In this work, σ_u is 552.66 MPa. By fitting $\sigma_{eq.G}$ and N_f with Basquin equation, the corresponding model parameters are obtained.

The traditional Smith−Watson−Topper (SWT) model is a stress−strain parameter-based model considering σ_m. For stress−life analysis, the influence of σ_m is considered by introducing σ_{max}. The formula of σ_{eq} is as follows:

$$\sigma_{eq.SWT}=\sqrt{\sigma_{max}\sigma_a} \tag{12}$$

Based on SWT model, a more general Walker model is proposed. Walker model adjusts the contribution of σ_{max} and σ_a to fatigue damage. The expression of σ_{eq} is as follows:

$$\sigma_{eq.W}=\sigma_a^{\gamma}\sigma_{max}^{1-\gamma} \tag{13}$$

where γ represents the fitting constant, which depends on the sensitivity of the material to σ_m. For most metal materials sensitive to σ_m, when 0.4 is taken, the model has good applicability.

Kwofie proposes an exponential form of σ_{eq} with σ_m and σ_u in consideration. The expression is as follows:

$$\sigma_{eq.K}=\sigma_a\exp\left(\alpha'\frac{\sigma_m}{\sigma_u}\right) \tag{14}$$

where α' represents the sensitivity of fatigue life to σ_m. Generally, 2 is preferable.

Under asymmetric stress control, σ_{eq} values of different life prediction models under different loading parameters are summarized in Table 5. Based on σ_{eq}, the comparison results of predicted life and tested life data of different models are shown in Fig. 15. It can be seen that only the fatigue life data points obtained by Kwofie model are in the range of double error band, so the prediction accuracy of Kwofie model is higher than that of the other three models. The fitting parameters of different life models are listed in Table 6.

(3) Equivalent life model based on energy method

Under symmetrical stress−strain controlled loading, the plasticity and total strain energy density

Table 5 Calculation results of σ_{eq}, ΔW_p and ΔW_t under half life

Sample	$\sigma_{eq.G}$/MPa	$\sigma_{eq.SWT}$/MPa	$\sigma_{eq.W}$/MPa	$\sigma_{eq.K}$/MPa	ΔW_p/(MJ·m^{-3})	ΔW_t/(MJ·m^{-3})
P05	316	315	316	321	0.07259	0.19804
P06	328	325	328	346	0.10952	0.25668
P07	341	334	339	371	0.12267	0.33748
P08	346	345	346	353	0.14722	0.31207
P09	360	355	358	379	0.22751	0.42738
P10	374	364	369	407	0.26283	0.5184
P11	377	375	376	384	0.30833	0.52771
P12	391	385	388	412	0.33762	0.60088
P13	407	394	399	443	0.41468	0.74376

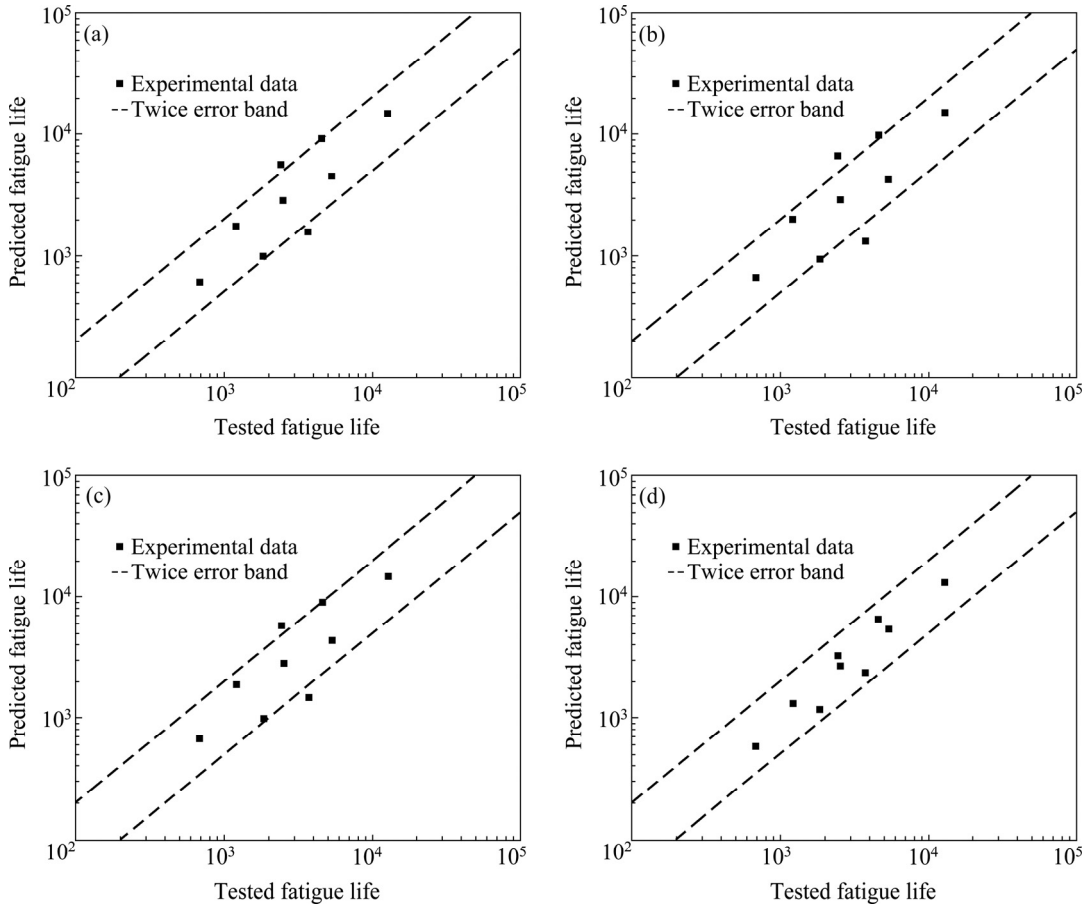

Fig. 15 Comparison of predicted and tested fatigue life data based on different models of σ_{eq}: (a) Goodman mode; (b) SWT model; (c) Walker model; (d) Kwofie model

at half-life of materials under cyclic loading have been proven to be able to predict fatigue life. Under asymmetric loading, due to the existence of σ_m, the equivalent life N_{eq} is introduced to replace the experimental life N_f in the life prediction model based on strain energy density. According to the σ_{eq} model, there are four main life models based on equivalent life [25], where,

$$N_{eq.G} = N_f\left(1-\frac{\sigma_m}{\sigma_u}\right)^{1/b}$$

$$N_{eq.SWT} = N_f\left(\frac{1-R_\sigma}{2}\right)^{1/(2b)}$$

$$N_{eq.W} = N_f\left(\frac{1-R_\sigma}{2}\right)^{(1-\gamma)/b}$$

and

$$N_{eq.K} = N_f \exp\left[\left(-\alpha'\frac{\sigma_m}{\sigma_u}\right)/b\right]$$

The definition of parameters in all models is consistent with the corresponding σ_{eq} formula.

Here, the equivalent life N_{eq} is used to replace the experimental life N_f, and the life prediction model of basic energy method is used to establish the relationship between N_{eq}, ΔW_p and ΔW_t, respectively. The parameters of life prediction models obtained by different models are given in Table 6. Figures 16 and 17 show the comparison results of predicted life and equivalent experimental life based on ΔW_p and ΔW_t, respectively. It can be seen that almost all predicted life points of the models are within 1.5 times error band. Therefore, the accuracy of the energy method life prediction model based on equivalent life theory is generally higher than that based on σ_{eq}.

(4) M-ESR model

By establishing the relationship between logarithmic fatigue life and that stress ratio, LIU et al [32] proposed the stress-based failure (SBF) model. The expression of the model is as follows:

$$N_f = e^{\gamma}e^{\eta R} \tag{15}$$

where γ and η are fitting parameters.

Table 6 Summary of life prediction model parameters based on σ_{eq}, ΔW_p and ΔW_t under half life

Model	σ_{eq}		ΔW_p		ΔW_t	
	σ_f'	b	k_f	α	k_f	α
Goodman	677.252	−0.07958	837.202	−0.97109	190.217	−0.7139
SWT	629.071	−0.07193	182.797	−0.81086	68.239	−0.60717
Walker	651.643	−0.07546	303.215	−0.86044	93.992	−0.63743
Kwofie	851.020	−0.10259	662.415	−0.9466	164.934	−0.69933

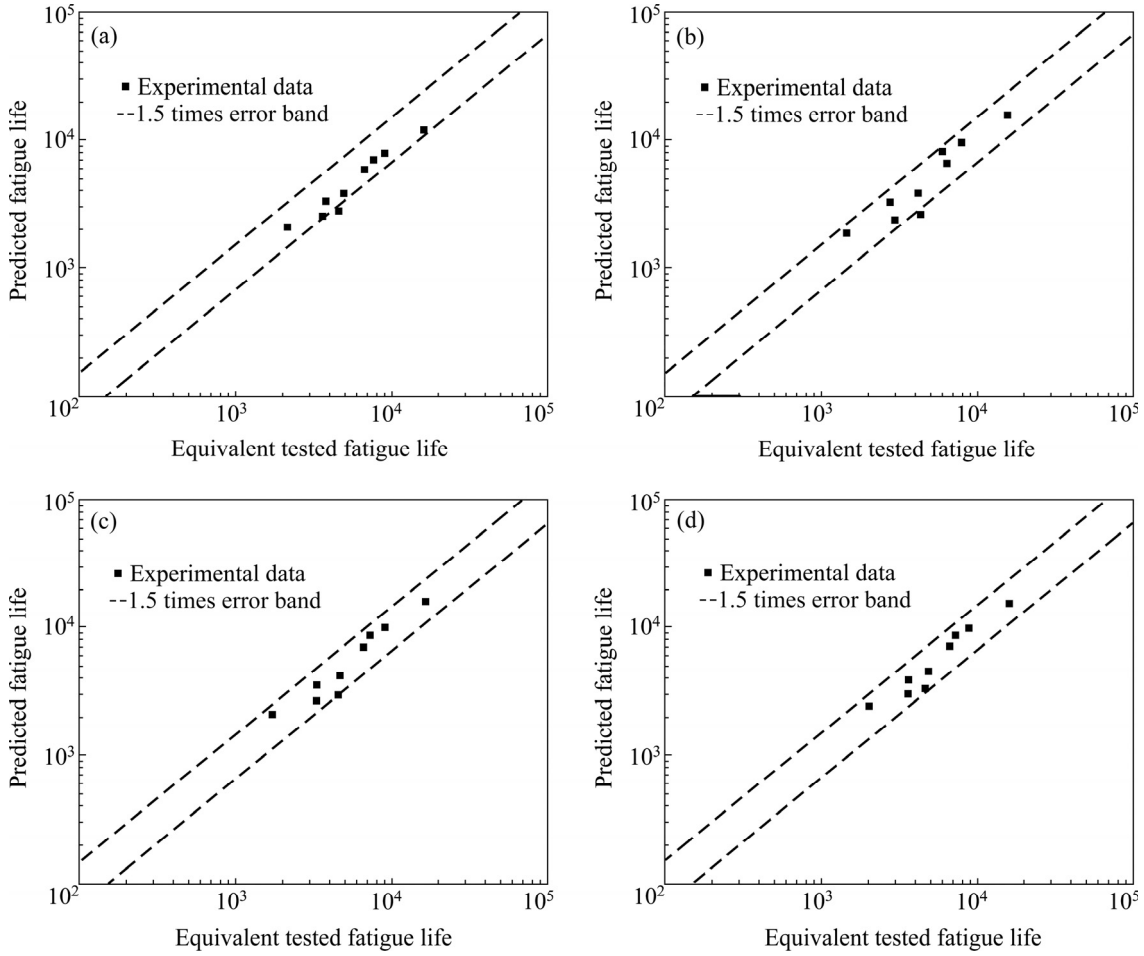

Fig. 16 Comparison of predicted and tested fatigue life data based on different models of ΔW_p: (a) Goodman model; (b) SWT mode; (c) Walker model; (d) Kwofie model

Because SBF model is unable to consider the influence of peak load, CHANG et al [33] built ESR (exponential stress ratio-related) model on this basis successfully. ESR model establishes the relationship between parameters γ and η and peak stress σ_p in exponential life model, and establishes a life prediction model considering peak stress and stress ratio. In this section, based on the idea of SBF and ESR model, the life prediction model considering σ_a and σ_m is constructed by establishing the relationship between parameters γ and η and σ_m in exponential life model:

$$N_f = e^{\gamma} e^{\eta\sigma_a} \tag{16}$$

The relationship between $\ln N_f$ and σ_a under different σ_m is shown in Fig. 18. It can be seen that the slope η of the fitting line of $\ln N_f$ and σ_a under different σ_m is approximately the same. Here, η= −0.021. The relationship between parameter γ and σ_m/σ_u is established:

$$\gamma = k\left(\frac{\sigma_m}{\sigma_u}\right) + c \tag{17}$$

Substituting the test data, k=−20.067 and c= 16.175. The expression of M-ESR model is as follows:

$$N_f = \exp[-0.021\sigma_a - 20.067(\sigma_m/\sigma_u) + 16.175] \tag{18}$$

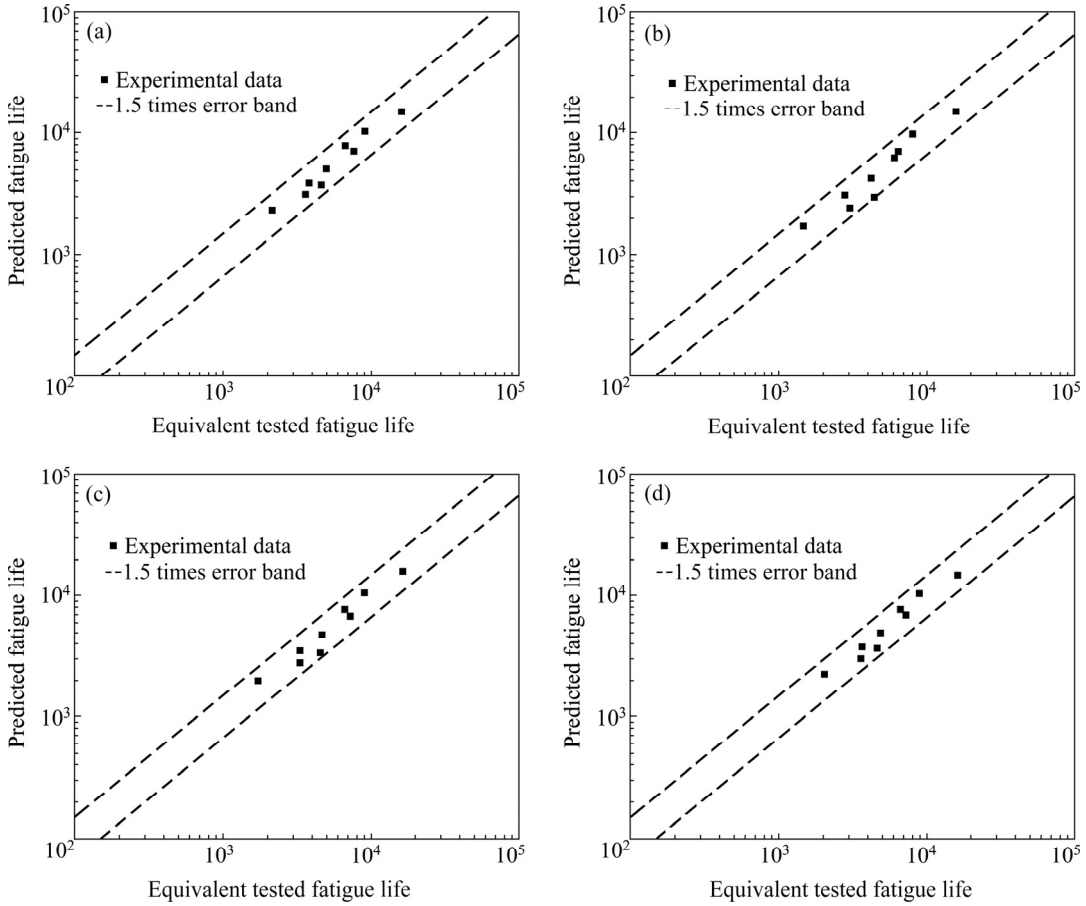

Fig. 17 Comparison of predicted and tested fatigue life data based on different models of ΔW_t: (a) Goodman model; (b) SWT mode; (c) Walker model; (d) Kwofie model

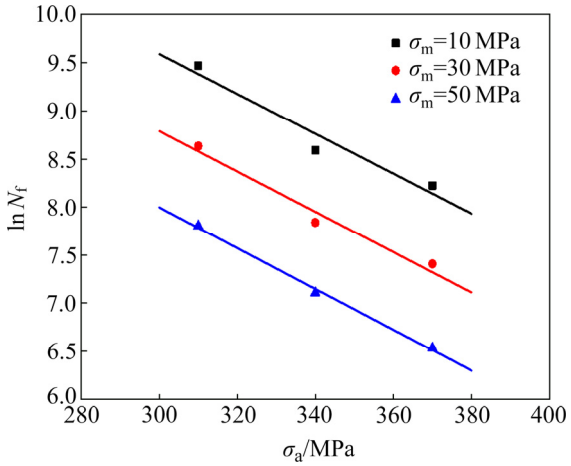

Fig. 18 The relationship between $\ln N_f$ and σ_a under different σ_m

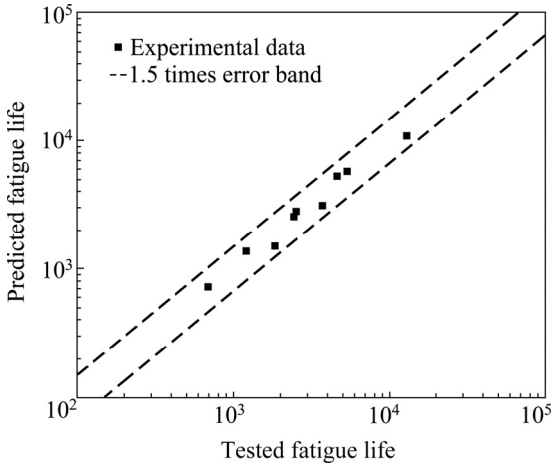

Fig. 19 Comparison of predicted and tested fatigue life data based on M-ESR model

Figure 19 shows that all life points predicted by M-ESR model are within the error band of 1.5 times, and the prediction accuracy of M-ESR model meets the requirements.

By comparing the relative average error (Δ_{mean}) of different models, the difference of prediction accuracy between different prediction models is quantitatively described. Relative average error Δ_{mean} is defined as follows:

$$\Delta_{mean}=\frac{1}{N}\sum_{i=1}^{N}\left|\frac{N_f^e-N_f^p}{N_f^e}\right|\times 100\% \quad (19)$$

As shown in Fig. 20(a), for the four main life prediction models, the accuracy of the equivalent

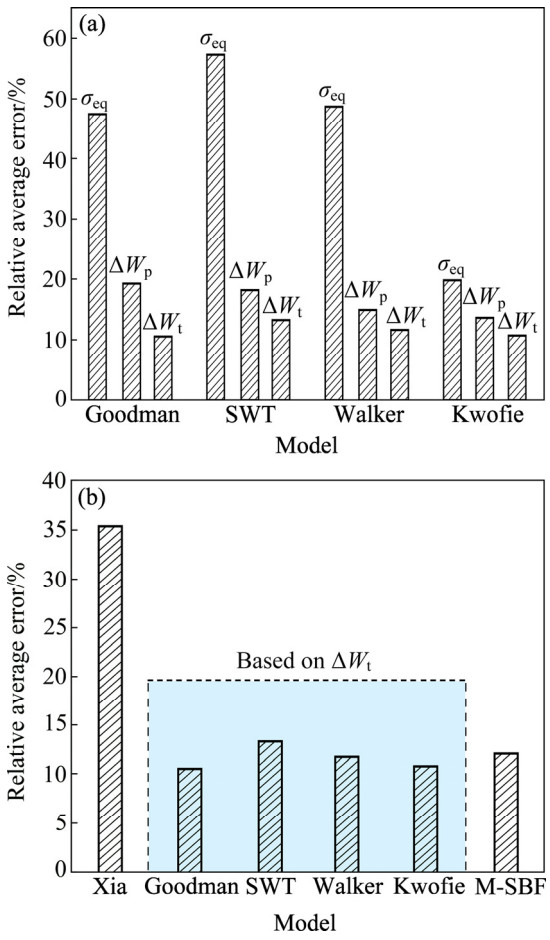

Fig. 20 Relative mean error of different models

life prediction model based on the total strain energy density ΔW_t at half-life is the highest, followed by the equivalent life prediction model based on the plastic strain energy density ΔW_p at half-life, and finally the life prediction model based on the equivalent stress. It can be seen that for asymmetric stress-controlled fatigue tests, the total strain energy density ΔW_t under steady cyclic loading can be used in the life prediction to accurately describe the total strain energy change during cyclic deformation of materials, so the prediction accuracy is the highest. Figure 20(b) shows that the prediction accuracy of the minimum ratcheting strain rate-dependent life prediction model (Xia model) is lower than that of the other five models, and the model needs to determine the mean ε_a and ratcheting strain rate. In addition, the relative average errors of four prediction models based on total strain energy density ΔW_t and M-BPM model Δ_{mean} are close, among which Goodman model has the highest accuracy. However, since M-BPM model can be directly applied to fatigue life prediction under given σ_m and σ_a, and the other four life prediction models depend on the total strain energy density ΔW_t at half-life of cyclic loading, M-BPM is most suitable for failure life prediction of zirconium−titanium−steel composite plate under asymmetric stress control cycle.

4 Conclusions

(1) Under the symmetrical stress control, ratcheting deformation is not obvious. Under the control of asymmetric stress, ratcheting strain increases rapidly with mean stress and stress amplitude. Under high stress amplitude, the effect of mean stress on ratcheting effect is more significant, and with the increase of loading cycles, the difference of ratcheting strain is enlarged. Ratcheting strain is more sensitive to the change of strain amplitude when the mean stress is higher.

(2) The evolution of strain energy density shows that the stress amplitude greatly increases the ratio of plastic strain energy to total strain energy, while the mean stress has limited influence. It can be seen that the stress amplitude increases the low cycle fatigue damage, while the mean stress increases the ratcheting damage.

(3) There are brittle metal compounds in vortex zone of titanium−steel interface due to explosive welding. Under fatigue loading, the structure breaks and cracks, and thus cracks initiate. After crack initiation, it diffuses around. Because the resistance of steel to crack propagation is significantly higher than that of titanium and zirconium, the crack propagates faster in titanium and zirconium, and preferentially leads to the fracture of transition layer and cladding.

(4) The analysis of different life prediction models shows that the life prediction model with the total strain energy density as the fitting object is more accurate. Besides, a life prediction model based directly on the mean stress and stress amplitude is proposed, and the predicted life points are located in the error band of 1.5 times.

Acknowledgments

The authors are grateful for the financial support from the National Natural Science Foundation of China (Nos. 51975271, 51675260, 51475223), and the Starting Research Fund of Nanjing Vocational University of Industry Technology, China (No. YK20-14-05).

References

[1] ZIDAN R A, TAKARA S, HEE A G, JENSEN C M. Hydrogen cycling behavior of zirconium and titanium–zirconium-doped sodium aluminum hydride [J]. Journal of Alloys and Compounds, 1999, 285(1/2):119−122.

[2] KIM W G, CHOE H C. Nanostructure and corrosion behaviors of nanotube formed Ti−Zr alloy [J]. Transactions of Nonferrous Metals Society of China, 2009, 19(4): 1005−1008.

[3] LIU Guang-lei, CAO Yu-hao, YANG Kun, GUO Wei, SUN Xiao-xuan, ZHAO Ling, SI Nai-chao, ZHOU Jian-zhong. Thermal fatigue crack growth behavior of $ZCuAl_{10}Fe_3Mn_2$ alloy strengthened by laser shock processing [J]. Transactions of Nonferrous Metals Society of China, 2021, 31(4): 1023−1030.

[4] DING Jun, KANG Guo-zheng, LIU Yu-jie, WANG Hai-lin. Uniaxial time-dependent cyclic deformation of 6061-T6 aluminium alloy [J]. The Chinese Journal of Nonferrous Metals, 2007, 17(12): 1993−1998. (in Chinese)

[5] CESCHINI L, MESSIERI S, MORRI A, SEIFEDDINE S, ZAMANI M. Effect of Cu addition on overaging behaviour, room and high temperature tensile and fatigue properties of A357 alloy [J]. Transactions of Nonferrous Metals Society of China, 2020, 30(11): 2861−2878.

[6] SZACHOGLUCHOWICZ I, SNIEZEK L, HUTSAYLYUK V. Low cycle fatigue properties of AA2519–Ti6Al4V laminate bonded by explosion welding [J]. Engineering Failure Analysis, 2016, 69: 77−87.

[7] FAN K, WANG G Z, XUAN F Z, TU S T. Effects of work hardening mismatch on fracture resistance behavior of bi-material interface regions [J]. Mater Design, 2015, 68: 186−194.

[8] RODRIGUEZ R I, JORDON J B, ALLISON P G, RUSHING T W, GARCIA L. Low-cycle fatigue of dissimilar friction stir welded aluminum alloys [J]. Materials Science & Engineering A, 2016, 654: 236−248.

[9] GOMEZ C, CANALES M, CALVO S, RIVERA R, VALDES J R, NUNEZ J L. High and low cycle fatigue life estimation of welding steel under constant amplitude loading: Analysis of different multiaxial damage models and in-phase and out-of-phase loading effects [J]. International Journal of Fatigue, 2011, 33(4): 578−587.

[10] CRUPI V, GUGLIELMINO E, RISITANO G, TAVILLA F. Experimental analyses of SFRP material under static and fatigue loading by means of thermographic and DIC techniques [J]. Composites Part B: Engineering, 2015, 77: 268−277.

[11] ROZUMEK D, MARCINIAK Z. Fatigue tests of bimetal zirconium−steel made by explosive welding [J]. Procedia Engineering, 2016, 160: 137−142.

[12] SZACHOGLUCHOWICZ I, SNIEZEK L, HUTSAYLYUK V. Low cycle fatigue properties laminate AA2519-TI6AL4V [J]. Procedia Engineering, 2015, 114: 26−33.

[13] PRAZMOWSKI M, ROZUMEK D, PAUL H. Influence of the microstructure on the fatigue cracks growth in the joint zirconium−steel made by explosive welding [J]. Solid State Phenomena, 2016, 258: 619−622.

[14] SNIEZEK L, SZACHOGLUCHOWICZ I, WACHOWSKI M, TORZEWSKI J, MIERZYNSKI J. High cycle fatigue properties of explosively welded laminate AA2519/AA1050/Ti6Al4V [J]. Procedia Structural Integrity, 2017, 5: 422−429.

[15] CHEN Kui-wai, PAN Su-ping, LIU Hui-qun, JIANG Yong. Effect of α phase morphology on fatigue crack growth behavior of Ti−5Al−5Mo−5V−1Cr−1Fe alloy [J]. Transactions of Nonferrous Metals Society of China, 2020, 30(9): 2459− 2471.

[16] MU Tong, SHI Guo-liang, ZHANG Kui, LI Xing-gang, LI Yong-jun, MA Ming-long, YUAN Jia-wei. High cycle fatigue behavior of T6-treated ZM51 alloy extrusion [J]. The Chinese Journal of Nonferrous Metals, 2020, 30(8): 1770−1780. (in Chinese)

[17] LUO Xiu-fang, YANG Ting-hui, LI Zheng, ZHANG Xin-ping, WANG Yang, DONG Cheng, HUANG Yang-jia, ZHANG Nian-su. Ratcheting behavior of AZ91D magnesium alloy under uniaxial cyclic stressing [J]. The Chinese Journal of Nonferrous Metals, 2009, 19(10): 1726−1732. (in Chinese)

[18] RAJPUROHIT R S, SUDHAKAR RAO G, CHATTOPADHYAY K, SRINIVAS N C S, SINGH V. Ratcheting fatigue behavior of Zircaloy-2 at room temperature [J]. Journal of Nuclear Materials, 2016, 477: 67−76.

[19] PAUL S K, STANFORD N, TAYLOR A, HILDITCH T. The effect of low cycle fatigue, ratcheting and mean stress relaxation on stress-strain response and microstructural development in a dual phase steel [J]. International Journal of Fatigue, 2015, 80: 341−348.

[20] YUAN X Y, YU W W, FU S C, YU D J, CHEN X. Effect of mean stress and ratcheting strain on the low cycle fatigue behavior of a wrought 316LN stainless steel [J]. Materials Science and Engineering A, 2016, 677: 193−202.

[21] PAUL S K, SIVAPRASAD S, DHAR S, TARAFDER S. Cyclic plastic deformation and damage in 304LN stainless steel [J]. Materials Science and Engineering A, 2011, 528(15): 4873−4882.

[22] CHANG L, ZHOU B B, MA T H, LI J, HE X H, ZHOU C Y. The difference in low cycle fatigue behavior of CP-Ti under fully reversed strain and stress controlled modes along rolling direction [J]. Materials Science and Engineering A, 2019, 742: 211−223.

[23] FANG T, KAN Q H, KANG G Z, YAN W Y. Uniaxial ratcheting and low-cycle fatigue failure of U75V rail steel [J]. Applied Mechanics and Materials, 2016, 853: 246−250.

[24] INCE A. A generalized mean stress correction model based on distortional strain energy [J]. International Journal of Fatigue, 2017, 104: 273−282.

[25] MAHTABI M J, SHAMSAEI N. A modified energy-based approach for fatigue life prediction of superelastic NiTi in presence of tensile mean strain and stress [J]. International Journal of Mechanical Sciences, 2016, 117: 321−333.

[26] CHANG L, ZHOU B B, MA T H, LI J, HE X H, ZHOU C Y. Comparisons of low cycle fatigue behavior of CP-Ti under stress and strain-controlled modes in transverse direction [J]. Materials Science and Engineering A, 2019, 746: 27−40.

[27] NING J, ZHANG L J, XIE M X, YANG H X, YIN X Q, ZHANG J X. Microstructure and property inhomogeneity investigations of bonded Zr/Ti/steel trimetallic sheet fabricated by explosive welding [J]. Journal of Alloys and Compounds, 2017, 698: 835−851.
[28] FUCHS H O, STEPHENS R I, SAUDERS H. Metal fatigue in engineering [J]. Journal of Engineering Materials & Technology, 1981, 103(4): 346.
[29] WU Zhi-rong, HU Xu-teng, SONG Ying-dong. Multi-axial fatigue life prediction model based on maximum shear strain amplitude and modified SWT parameter [J]. Journal of Mechanical Engineering, 2013, 49(2): 59−66. (in Chinese)
[30] Al-RUBAIE K S. A general model for stress-life fatigue prediction [J]. Materialwissenschaft und Werkstofftechnik, 2008, 39(6): 400−406.
[31] KWOFIE S, RAHBAR N. An equivalent driving force model for crack growth prediction under different stress ratios [J]. International Journal of Fatigue, 2011, 33(9): 1199−1204.
[32] LIU Y, KANG G, GAO Q. Stress-based fatigue failure models for uniaxial ratchetting–fatigue interaction [J]. International Journal of Fatigue, 2008, 30(6): 1065−1073.
[33] CHANG L, WEN J B, ZHOU C Y, ZHOU B B, LI J. Uniaxial ratcheting behavior and fatigue life models of commercial pure titanium [J]. Fatigue & Fracture of Engineering Materials & Structures, 2018, 41(1/2/3): 2024−2039.

锆−钛−钢复合板的低周疲劳行为

周彬彬[1]，于 鹏[1]，常 乐[2,3]，周昌玉[2,3]，业 成[4]，张伯君[4]

1. 南京工业职业技术大学 工程技术实训中心，南京 210023；
2. 南京工业大学 机械与动力工程学院，南京 211816；
3. 江苏省极端承压装备设计与制造重点实验室，南京 210028；
4. 南京市锅炉压力容器检验研究院 技术研发部，南京 210028

摘 要：研究锆−钛−钢复合板在对称和非对称应力控制下的低周疲劳行为，详细讨论平均应力和应力幅值对循环变形、棘轮效应和损伤机理的影响。结果表明，在对称应力控制下，观察到正向棘轮变形；在非对称应力控制下，棘轮应变随平均应力和应力幅值的增加而快速增加；在高应力幅值下，平均应力影响更为显著。此外，通过研究应变能密度，发现应力幅值主要促进疲劳损伤，而平均应力则导致棘轮损伤。另外，通过断口观察可以看出，裂纹萌生于界面处的脆性金属化合物中，且钢材抗裂纹扩展的阻力更高。最后，详细讨论考虑棘轮效应的寿命预测模型精度，并提出一种直接基于平均应力和应力幅值的高精度寿命预测模型。

关键词：锆−钛−钢复合板；低周疲劳行为；疲劳损伤；平均应力；棘轮效应；寿命预测模型

(Edited by Bing YANG)